Applied Catalysis B: Environmental 328 (2023) 122520

Contents lists available at ScienceDirect

Applied Catalysis B: Environmental

journal homepage: www.elsevier.com/locate/apcatb

Hollow-structured $BaTiO_3$ nanoparticles with cerium-regulated defect engineering to promote piezocatalytic antibacterial treatment

Junwu Wei [a], Jing Xia [a], Xing Liu [b], Pan Ran [a], Guiyuan Zhang [a], Chaoming Wang [b], Xiaohong Li [a,*]

[a] College of Medicine, Key Laboratory of Advanced Technologies of Materials (Ministry of Education), Southwest Jiaotong University, Chengdu 610031, China
[b] Applied Mechanics and Structure Safety Key Laboratory of Sichuan Province, School of Mechanics and Aerospace Engineering, Southwest Jiaotong University, Chengdu, Sichuan 610031, China

ARTICLE INFO

Keywords:
Piezoelectric potential
Hollow structure
Defect engineering
Piezocatalytic activity
Antibacterial therapy

ABSTRACT

The low efficiency of mechanical energy capture and insufficient active sites are the main obstacles of piezocatalytic therapy. Herein, cerium (Ce)-doped hollow $BaTiO_3$ (hBT_{Ce}) nanoparticles (NPs) were developed to improve the piezocatalytic effect through simultaneously hollow structure and defect engineering. hBT NPs were prepared through precipitation of TiO_2 layers on SiO_2 NP templates, transformation into $BaTiO_3$ layer, and simultaneous removal of SiO_2 cores. The hollow structure exhibits a stronger piezoresponse than solid NPs, and the piezoelectric coefficient increases nearly 2.6 times. The Ce doping enhances polarization, oxygen vacancy formation and electron/hole separation, and reduces the band gap of hBT_{Ce} NPs. Both the strong piezoelectric current and abundant generation of reactive oxygen species from hBT_{Ce} under ultrasonication contribute to significant destructions of planktonic bacteria and biofilms. Thus, this study demonstrates the Ce-regulated defect engineering and hollow structure of piezoelectric NPs are effective to promote polarization, piezoelectric potential and piezocatalytic antibacterial therapy.

1. Introduction

Bacterial infection afflicts millions of people every year and has become a major threat to human health. Antibiotic treatment has made significant achievements in combating bacterial infection, but usually exhibits inevitable shortcomings in immune system impairment, bacterial resistance evolution, and environmental pollution [1]. Non-antibiotic agents, such as antimicrobial peptides, germicidal metallic ions and cationic polymers have shown intrinsic bactericidal activity through disrupting bacterial membrane and interrupting metabolism process. But these bactericidal agents usually reveal systemic toxicity and tend to require a long treatment [2]. Alternatively, triggerable antimicrobial strategies are emerging as one effective therapeutic modality with a high spatiotemporal specificity, and are commonly processed by using exogenous stimuli, such as light, ultrasound, magnetic field, electricity, and ionizing irradiation. These systems produce heat and reactive oxygen species (ROS) to generate oxidative stress and lipid peroxidation, damage proteins and DNA molecules and eventually induce bacterial death [3]. Photodynamic (PDT) and photothermal therapies (PTT) are widely studied under light activation, but suffer from insurmountable problems such as low tissue penetration depth, phototoxicity and hyperthermia-induced damage to normal tissues [4]. Sonodynamic therapy (SDT) benefits from noninvasive and nonradiative nature of ultrasound with deep tissue penetration and high intensity controllability. Versatile organic and inorganic sonosensitizers have been explored, but traditional organic sonosensitizers suffer from poor hydrophobicity, low bioavailability and rapid excretion. Inorganic sonosensitizers have relatively low quantum yields of ROS due to the easy recombination of electrons (e^-) and holes (h^+) [5].

Electrical stimulation has been demonstrated to be another efficient way to combat bacterial infection. Dependent on the stimulation magnitude and duration, electrical field generates electroporation and electrodynamic effect to reduce microbial growth. A high electric field (1–10 kV/cm) may change the organization of cell membranes and disrupt metabolic processes through electroporation and ROS may be produced from water decomposition under a certain voltage [6]. The disinfection mechanism could prevent the emergence of

* Corresponding author.
E-mail address: xhli@swjtu.edu.cn (X. Li).

https://doi.org/10.1016/j.apcatb.2023.122520
Received 9 November 2022; Received in revised form 6 January 2023; Accepted 22 February 2023
Available online 24 February 2023
0926-3373/© 2023 Elsevier B.V. All rights reserved.

multidrug-resistant bacteria and the therapeutic efficacy is not relied on the biological microenvironment characteristics, such as O_2 and H_2O_2 contents in the other dynamic therapies [7]. In addition to external direct or alternating current power supplies, triboelectric and piezoelectric generators have been developed through the conversion of mechanical energy into electric powers. Wang et al. prepared a triboelectric nanogenerator bandage to convert the mechanical stress of skins into an alternating electric field, which was connected by wires at both ends of the wound to promote the migration, proliferation and differentiation of fibroblasts [8]. However, the self-powered electrodynamic therapy is highly influenced by individual mechanic stress and performed by inserting bulk electrodes at the lesion site, thus the invasive process may inevitably cause secondary damage to the wound tissues. In this context, piezocatalytic therapy has been developed for in situ generation of an internal electric field in piezoelectric materials for antibacterial applications. The external mechanical stress could activate piezoelectric materials with non-centrosymmetric structure, drive e^-/h^+ separation to the opposite surface, and the separated charges further react with surrounding O_2 and H_2O to produce ROS [9]. However, for the typical piezoelectric materials such as $BiFeO_3$, $BaTiO_3$ and ZnO_2, the low-voltage electric polarization even under a high ultrasonic power or stirring speed shows a low carrier concentration and charge separation efficiency, directly leading to a low piezocatalytic efficiency [10].

High piezoelectric properties and abundant catalytic active sites are essential for improving ROS generation by piezocatalytic materials [11]. Several routes have been pursued to enhance piezocatalytic properties through polarization treatment (e.g., high voltage, high temperature, and strong straining), morphology and phase boundary controls [12]. For example, the gadolinium doping of $BaTiO_3$ nanoparticles (NPs) induced lattice distortion and the surface reconstruction of $BaTiO_3$ NPs induced lattice mismatch to enhance piezoelectric properties [13]. Flexible $BaTiO_3$ nanosheets were used to improve the piezoelectric properties by increasing the shape variable under pressure [14]. In addition to piezoelectric responsiveness, the specific surface area, active site exposure, and defect characteristics also play important roles in piezocatalytic activity. Among them, defect engineering is an effective method to regulate the charge distribution and catalytic performance of piezoelectric materials. In particular, defect-induced atomic vacancies could improve the separation of e^-/h^+ pairs and enhance the adsorption of O_2 and H_2O to reduce their redox energy barrier [15]. Currently defects are mostly created by chemical etching or high-temperature annealing, and these directly formed atomic vacancies on the surface tend to suppress the spontaneous polarization and reduce the carrier concentration, causing a negative effect on the piezoelectric response. Liu at al. introduced oxygen vacancies (OVs) into $BaTiO_3$ nanobelt surface through vacuum heating to activate O_2 and consequently enhance the piezocatalytic activity, but the piezoelectric response was weakened with increasing the OV content [16]. Therefore, the weak piezoelectric performance is still one of the key factors limiting the piezocatalytic efficiency, and it is particularly important to modulate the generation of appropriate OVs without sacrificing the piezoelectric response.

Herein, hollow-structured and cerium (Ce)-doped $BaTiO_3$ (hBT_{Ce}) NPs were developed to promote ROS generation efficiency under ultrasonication through simultaneously hollow structure and defect engineering. Scheme 1a illustrates the fabricating procedure of hBT_{Ce} NPs through precipitation of TiO_2 layer on SiO_2 NP templates, transformation into $BaTiO_3$ layer and simultaneous removal of SiO_2 cores after reaction with $Ba(OH)_2$ in the presence of $Ce(NO_3)_3$•6 H_2O. Hollow-structured NPs are accompanied with high specific surface areas and discrete pores to provide abundant accessible sites for catalytic reactions. Compared with typical bulk materials, the hollow structure allowed a high flexibility and large deformation under ultrasonication, and the short diffusion path of ion transmissions and high piezoelectric potential would increase the piezocatalytic performance. In addition, Ce-doped hBT_{Ce} NPs not only promoted polarization, but the induced OVs could also provide electron trapping sites and promote the separation of e^-/h^+ pairs from the band structure under ultrasonication. hBT_{Ce} NPs provided a stronger adsorption capacity for O_2 and H_2O molecules and increased the efficiency of ROS generation (Scheme 1b). Thus, the Ce-regulated defect engineering and hollow structure endowed hBT_{Ce} NPs with a high piezocatalytic efficiency for antibacterial and antibiofilm treatment (Scheme 1c).

2. Experimental section

2.1. Materials

Tetraethyl orthosilicate, titanium isopropoxide (TTIP), Ba $(OH)_2$•8 H_2O, $Ce(NO_3)_3$•6 H_2O, methylene blue (MB), Nafion solution, and 3-(4,5-dimethylthiazol-2-yl)− 2,5-diphenyltetrazolium bromide (MTT) were obtained from Aladdin Reagents Company (Shanghai, China). $DiBAC_4(3)$, terephthalic acid, and 1,3-diphenylisobenzofuran (DPBF) were procured from Sigma-Aldrich (St. Louis, MO, USA). Methicillin-resistant *Staphylococcus aureus* (MRSA) and *Pseudomonas aeruginosa* (*P. aeruginosa*) were received from the Chinese Medical Culture Collection Center (Beijing, China). All other chemicals were of analytical grade and obtained from Kelong Regents Company (Chengdu, China) unless otherwise indicated.

2.2. Preparation of hBT and hBT_{Ce} NPs

Scheme 1a illustrates the preparation of hBT_{Ce} NPs from SiO_2 NPs through creating Ce-doped $BaTiO_3$ layers and etching SiO_2 cores. Briefly, to a mixture of ethanol (40 mL), distilled water (6.4 mL), and ammonia (8.46 mL) was added dropwise 4.33 mL of tetraethyl

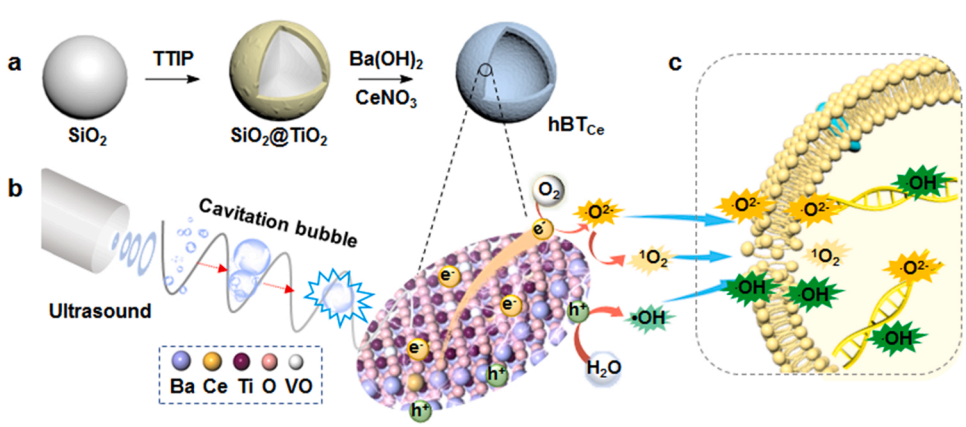

Scheme 1. Schematic illustration of the preparation process and antibacterial mechanism of hBT_{Ce} NPs. (a) hBT_{Ce} NPs were prepared through precipitation of TiO_2 layer on SiO_2 NPs, followed by transformation into $BaTiO_3$ layer and removal of SiO_2 cores. (b) Ce dopants promoted polarization and induced OVs to enhance the separation of e^-/h^+ pairs in hBT_{Ce} NPs under ultrasonication. (c) The generated piezoelectric field may interrupt bacterial membranes and produced ROS to destroy bacteria.

orthosilicate, followed by reaction for 3 h at 60 °C [17]. The collected SiO_2 NPs were washed with water, dispersed into ethanol (18 mL) and acetonitrile (6 mL), and then mixed with TTIP (3.6 mL) for 6 h at 5 °C [18]. The collected SiO_2 @TiO_2 NPs were dispersed in ethanol (20 mL) and mixed with 30 mL of $Ba(OH)_2$ (0.05 M) and $Ce(NO_3)_3$•6 H_2O (2 mM) solutions. The mixture was autoclaved for 6 h at 160 °C, and white precipitates were rinsed with ethanol, vacuum-dried overnight, and calcined at 900 °C for 3 h to obtain hBT_{Ce} NPs [19]. hBT NPs were prepared without inoculation of $Ce(NO_3)_3$•6 H_2O followed by the same process. For comparison, BT NPs were prepared through mixing Ba $(OH)_2$ •8 H_2O (0.158 g, 0.5 mmol) and TTIP (0.142 g, 0.5 mmol) in 25 mL of distilled water and 3 mL of ammonia (30%), followed by autoclaving at 160 °C for 12 h, vacuum drying and calcination at 900 °C for 3 h [20].

2.3. NP characterization

The surface morphology of NPs was observed by scanning electron microscopy (SEM; FEI Quanta 200, The Netherlands). The hollow structure and crystal lattice spacing of hBT_{Ce} NPs were examined by transmission electron microscopy (TEM; JEOL JEM-2100 F, Japan), and elemental mapping was performed by energy dispersive X-ray spectrometry (EDX). The crystalline pattern was measured by X-ray diffractometry (XRD; Philips X′Pert PRO, The Netherlands) and the surface electron state of NPs was detected by X-ray photoelectron spectroscopy (XPS; Thermo Scientific Escalab 250X, USA). The defect introduction was assayed by Raman spectroscopy (Horiba LabRAM HR-800, Japan) by using a laser with a wavelength of 532 nm. Piezoresponse force microscopy (PFM; Bruker MultiMode 8, USA) was used to characterize the piezoelectric performance of NPs. NPs were pretreated at 90 °C for 12 h, and the Brunauer-Emmett-Teller (BET) specific surface area and Barrett–Joyner–Halenda (BJH) pore size were analyzed via nitrogen adsorption-desorption by using a specific surface area and pore structure analyzer (Micromeritics Tristar II 3020, USA). The absorption profiles of dye degradation were recorded by ultraviolet-visible (UV-Vis) spectroscopy (Shimadzu UV-3600, Japan), and the UV–Vis diffuse reflectance spectra was measured by spectrophotometer (Hitachi U-4100, Japan) with an integrating sphere.

2.4. Piezocatalytic activity of hBT_{Ce} NPs

Piezocatalytic activities of BT, hBT, BT_{Ce}, and hBT_{Ce} NPs were measured from the generation of ROS and the subpopulation of •OH, $^1O_2$ and $•O^{2-}$, and the whole testing was carried out in the dark and an water bath (25 °C) to avoid the influence of photolysis and thermocatalysis. Briefly, 5 mg of NPs were dispersed in 5 mL of MB solution (10 μg/mL) overnight to ensure an absorption equilibrium, followed by 10 min of ultrasonication (1.5 W/cm^2, 1 MHz, 50% duty cycle). The supernatant was collected by centrifugation, and the degradation rate of MB was measured from absorbance values at 664 nm by UV-Vis spectroscopy to reflect the ROS generation [21]. To measure the generation of $^1O_2$ and $•O^{2-}$, 1 mL of NP suspension (25 μg/mL) was mixed with 20 μL of DPBF solution (1 mg/mL) as a probe, followed by ultrasonication for 10 min. The change of DPBF concentration was calculated from UV−Vis absorption intensities at 410 nm [22]. To detect •OH generation, terephthalic acid (0.25 mg) was used as a fluorescent probe and added into 3 mL of NaOH solution (2 mM), followed by mixing with 3 mL of NP suspensions (200 μg/mL) and ultrasonication for 10 min. The fluorescence intensity of the supernatant was determined by fluorescence spectrophotometry (Hitachi F-7000, Japan) at the excitation wavelength of 315 nm [23].

2.5. Ultrasonic electrochemistry measurement of hBT_{Ce} NPs

The piezoelectric current, electrochemical impedance spectroscopy (EIS) and Motty-Schottky potential were examined on an electrochemical workstation (Versa STAT 3 F, USA). Briefly, 10 mg of NPs were dispersed into the mixture of 0.5 mL of acetone and 20 μL of Nafion solution (5%). After ultrasonication for 30 min, 20 μL of the mixture was pipetted on a glassy carbon electrode in a diameter of 5 mm, and then air-dried for 12 h [24]. The sample-loaded electrode, platinum sheet (1 × 1 cm^2) and saturated Ag/AgCl electrode were used as the working, auxiliary and reference electrodes, respectively. Piezoelectric current was determined in Na_2SO_4 solution (0.5 M) as the reaction electrolyte under ultrasonication. Mott-Schottky plots were measured at 1000 Hz, and the step voltage was 0.02 V. EIS was recorded with an alternating current of 5 mV amplitude in the frequency range of 0.1–10^5 Hz.

2.6. First-principles calculation of hBT_{Ce} NPs

To reflect the electron exchange-correlation energy, the band structure and density of states (DOS) of BT and hBT_{Ce} NPs were calculated through density functional theory (DFT) by using CASTEP software [25]. The electronic correction function was executed with GGA and PBE. The plane-wave cutoff energy was set as 571.4 eV, and a 4 × 4 × 4 k-point was used for geometry optimizations of the Brillouin zone. The criteria for convergence of energies and forces were 10^{-5} eV and 0.02 eV Å^{-1}, respectively.

To clarify H_2O adsorption, spin-polarized calculations were carried through DFT [26]. The original bulk structures of BT_{Ce} were constructed from the reference by replacing 4% Ba with Ce. Based on the most stable bulk structure, several (001) surfaces were cleaved to consist with the experimental results, and the following simulation was performed on the most stable one. The defect surface with OVs was constructed by removing surface oxygen atoms from BT_{Ce} NPs. For the slab model, the vacuum was set to 15 Å to separate the neighboring layers interactions. The *k*-mesh sampling was set to be (4 × 4 × 1) and the atoms in the lower 4 layer were fixed while the rest atoms were totally relaxed during the optimization process. The adsorption energy (ΔE) of H_2O molecules was defined as Eq. (1): [11].

$$\Delta E = E(\text{Surf-H}_2\text{O}) - E(\text{Surf}) - E(\text{H}_2\text{O}) \quad (1)$$

where E(Surf-H_2O), E(Surf), and E(H_2O) are the energies of the adsorbed model, the surface of pristine hBT or hBT_{Ce}, and the isolated H_2O.

2.7. Simulation of piezoelectric potential

Piezoelectric potential of BT and hBT NPs were simulated through finite element method (FEM) by using COMSOL Multiphysics 5.6 software [27]. The polarization of NPs model was aligned along the z axis of global coordinate, while the central plane was fixed perpendicularly to z axis and grounded. The simulated pressure on NPs was set between 10^5 and 10^8 Pa [12], and the piezoelectric potential distribution on the surface of NPs was obtained by using the PARDISO solver.

2.8. Antibacterial efficacy of hBT_{Ce} NPs

The piezocatalytic antibacterial efficacy of hBT_{Ce} NPs under ultrasonication (hBT_{Ce}/US) was examined after incubation with P. aeruginosa and MRSA as examples of Gram-positive and Gram-negative bacteria, by using BT/US and hBT/US as controls [28]. Briefly, 100 μL of bacterial suspension (1 × 108 CFU mL−1) was inoculated into each well of a 96-well tissue culture plate (TCP) and added with 100 μL of NP suspensions (100, 50, 25, 12.5, 6.25, and 3.13 μg/mL). After ultrasonication for 5 min, optical densities at 590 nm (OD590) were measured by a microplate reader (Bio-Tek Elx-800, USA) to assess the minimum inhibitory concentration (MIC) [28]. In another batch of experiment, 100 μL of NP suspensions (50 μg/mL) was mixed with 100 μL of bacterial suspensions (2 × 106 CFU mL−1), followed by

ultrasonication for 5 min. After incubation in Luria-Bertani media at 37 °C for 12 h, bacterial colonies were counted on agar plates to determine the antibacterial rate of NPs. In addition, bacteria were retrieved and fixed with 2.5% glutaraldehyde for 2 h and the morphologies were observed under SEM.

The effect of piezoelectric output on the cell membrane potential of bacteria was measured by using DiBAC4(3) as a fluorescent probe [29]. Briefly, 20 μL of DiBAC4(3) (5 μM) and 200 μL of bacterial suspensions with OD590 of 0.3 were mixed for 30 min at 37 °C. The mixture was added with NP suspensions (25 μg/mL) and ultrasonicated for 5 min, and the fluorescence intensities were measured at the excitation wavelength of 490 nm.

2.9. Antibiofilm efficacy of hBT_{Ce} NPs

The antibiofilm effect was investigated in terms of biofilm mass, bacterial viability and morphology observation after treatment with BT/US, hBT/US and hBT_{Ce}/US [30]. Briefly, 200 μL of MRSA in Luria-Bertani media (1×10^8 CFU/mL) was cultured in 96-well TCPs at 37 °C for 48 h. The unbound bacteria were rinsed with PBS, and the retrieved biofilm was treated for 12 h with 100 μL of NP suspensions (25 μg/mL). After ultrasonication for 5 min, biofilms were washed with PBS and incubated with 200 μL of crystal violet solution (0.1%). The stained biofilm was washed with PBS and dispersed into 1.0 mL of ethanol (95%), and the remaining biofilm was detected by measuring the absorbance at 590 nm [30]. To detect bacterial viability, the treated biofilms were dispersed to collect bacteria for plate counting, and stained by using a bacterial live/dead staining kit (Molecular Probe, Eugene, OR, USA) for confocal laser scanning microscope (CLSM, Leica TCS SP2, Germany) examination. The treated biofilm was fixed in with 2.5% glutaraldehyde for 2 h, and their morphology was observed by SEM.

2.10. Cytotoxicity testing of hBT_{Ce} NPs

The cell toxicity was examined on mouse embryonic fibroblast cell (NIH-3T3) after treatment with hBT_{Ce} NPs [31]. Briefly, cells were received from the American Type Culture Collection (Rockville, MD, USA) and cultured in Dulbecco's modified Eagle's medium containing 10% fetal bovine serum (Gibco BRL, Grand Island, NY, USA). Cells were plated into 96-well TCPs at 3000 cells/well and treated with NPs of serial concentrations (800, 400, 200, 100, 50, and 25 μg/mL). After incubation for 24 h, cells were cultured in 100 μL of fresh media containing 5 mg/mL of MTT. After adding 100 μL of dimethyl sulfoxide, the absorbance of each well at 490 nm was measured on a microplate reader.

2.11. Statistical analysis

Data are expressed as the mean ± standard deviation. When needed, analysis of variance (ANOVA) was used to compare multiple groups, and two-tailed Student's *t*-test was used to identify statistical differences between the two groups. The probability value (p) less than 0.05 was thought to be statistically significant.

3. Results and discussion

3.1. Characterization of hBT_{Ce} NPs

Scheme 1a illustrates the preparation process of hBT_{Ce} NPs. Amorphous TiO_2 layers were deposited on SiO_2 NPs by the sol−gel method using TTIP as precursor, and then in situ transformed into $BaTiO_3$ by the hydrothermal method after reaction with $Ba(OH)_2$. In the meantime, SiO_2 NPs were etched by $Ba(OH)_2$ solution to prepare hBT NPs, and cerium nitrate was inoculated in the $BaTiO_3$ transformation to obtain hBT_{Ce} NPs. Thus, $Ba(OH)_2$ solution not only acted as a reactant with the TiO_2 shell to generate $BaTiO_3$ layer, but also provided a mild alkaline environment to gradually remove SiO_2 cores to reduce the damage to the structural integrity of hollow NPs [18]. Fig. 1a shows SEM morphologies of SiO_2, SiO_2 @TiO_2, hBT, and hBT_{Ce} NPs. The average diameter of SiO_2 NPs was about 180 nm and slightly increased to 200 nm after deposition of TiO_2 layer. The transformation into $BaTiO_3$ layer and removal of SiO_2 cores led to formation hBT_{Ce} NPs with a hollow structure, rough surface and average size of 200 nm. For comparison, BT NPs were prepared from $Ba(OH)_2$ •8 H_2O and TTIP and showed an average size of 192 nm. TEM observation of hBT_{Ce} NPs showed a hollow structure with a dense shell of around 10 nm thick (Fig. 1b). Fig. 1c shows high-resolution TEM images of hBT and hBT_{Ce}-4 NPs, indicating a high crystallinity with crystal planes of (110). Compared with that of hBT (2.84 nm), the lattice fringe spacing of hBT_{Ce}-4 NPs exhibited a slight variation (2.86 nm), suggesting the lattice expanded slightly after Ce doping. The EDX spectra displayed a trace amount of Si element in hBT_{Ce}-4 NPs (Fig. 1d), suggesting that SiO_2 cores have been etched away by alkaline solution treatment. The EDX element mapping images indicated that Ba, Ti, O and Ce elements were distributed on the out layer (Fig. 1e), indicating the homogeneous doping of Ce on the NP shell.

Fig. 1f shows XRD patterns of BT, hBT, BT_{Ce}, and hBT_{Ce} NPs, which corresponded to the tetragonal phase of $BaTiO_3$ with non-centrosymmetric crystal structure (JCPDS card: 79–2263). Obvious secondary splits appeared in the (200)/(002) diffraction peak at ~ 45°, indicating that BT and hBT NPs had a good tetragonal phase structure. The splitting diffraction peak became obscured with the increase of Ce doping levels, suggesting the coexistence of tetragonal and pseudo-cubic structure phases [32]. The diffraction peaks gradually shifted to a lower angle, indicating the lattice expansion and crystal structure distortion [33]. The moderate lattice expansion could enhance the polarization of $BaTiO_3$ to improve the piezoelectric response. Wang et al. also reported that gadolinium-doped BT showed an incomplete peak splitting of (002) and (200) crystal planes and the diffraction peeks shifted toward a low degree with gadolinium doping [13]. It should be noted that CeO_2 had characteristic peaks at 28.5°, 32.9°, 47.4°, and 56.8° (JCPDS No. 34–0394), while hBT_{Ce} NPs showed no obvious diffraction peaks of CeO_2. It was indicated that Ce was completely integrated into the $BaTiO_3$ skeleton without formation of CeO_2 crystals, and the Ce doping had no influence on the crystalline phase and purity of BT NPs.

Raman spectroscopy was employed to investigate the effect of Ce doping on the crystallographic structure of hBT_{Ce} NPs. It should be noted that there was no absorption peak in the Raman spectra of normal cubic $BaTiO_3$ due to the centrosymmetric feature for each ion [34]. As shown in Fig. 1g, tetragonal $BaTiO_3$ showed five Raman absorption peaks at 18, 260, 307, 515, and 720 cm^{-1} [35]. There was no characteristic peak of TiO_2 in the Raman spectra, indicating that all the TiO_2 was transformed into BT. The peaks at 307 cm^{-1} [E(TO+LO), B_1] and 720 cm^{-1} [A_1(LO), E (LO)] were the characteristic absorption of tetragonal $BaTiO_3$, confirming the induced spontaneous polarization at the order–disorder transition [34]. The peak at 186 cm^{-1} [A_1 (TO)] indicated the small size of NPs, and peaks at 260 [A_1 (TO)] and 515 cm^{-1} [A_1 (TO)] suggested the defect-induced local Ti^{4+} disorder [36]. Compared with BT and hBT NPs, an additional peak at 830 cm^{-1} for hBT_{Ce} NPs was caused by the internal deformation of TiO_6 octahedron induced by the substitution of Ce^{3+} on the equivalent Ba site. This further proved that the doped Ce^{3+} occupied the Ba^{2+} site and induced the lattice distortion [37]. In addition, BT_{Ce}-4 showed much higher peak strength than hBT_{Ce}-4, implying that BT_{Ce}-4 had more defects than hBT_{Ce}-4 NPs. Compared with hollow NPs, there were more defects and lattice distortion in thick solid NPs at the same Ce concentration [38].

3.2. Effect of hollow structure on the piezocatalytic activity of hBT_{Ce} NPs

Ultrasonication would produce a lot of cavitation bubbles, which then developed further and finally collapsed. The bubble rupture would generate pressures up to $10^5 - 10^8$ Pa [39], and the resulting

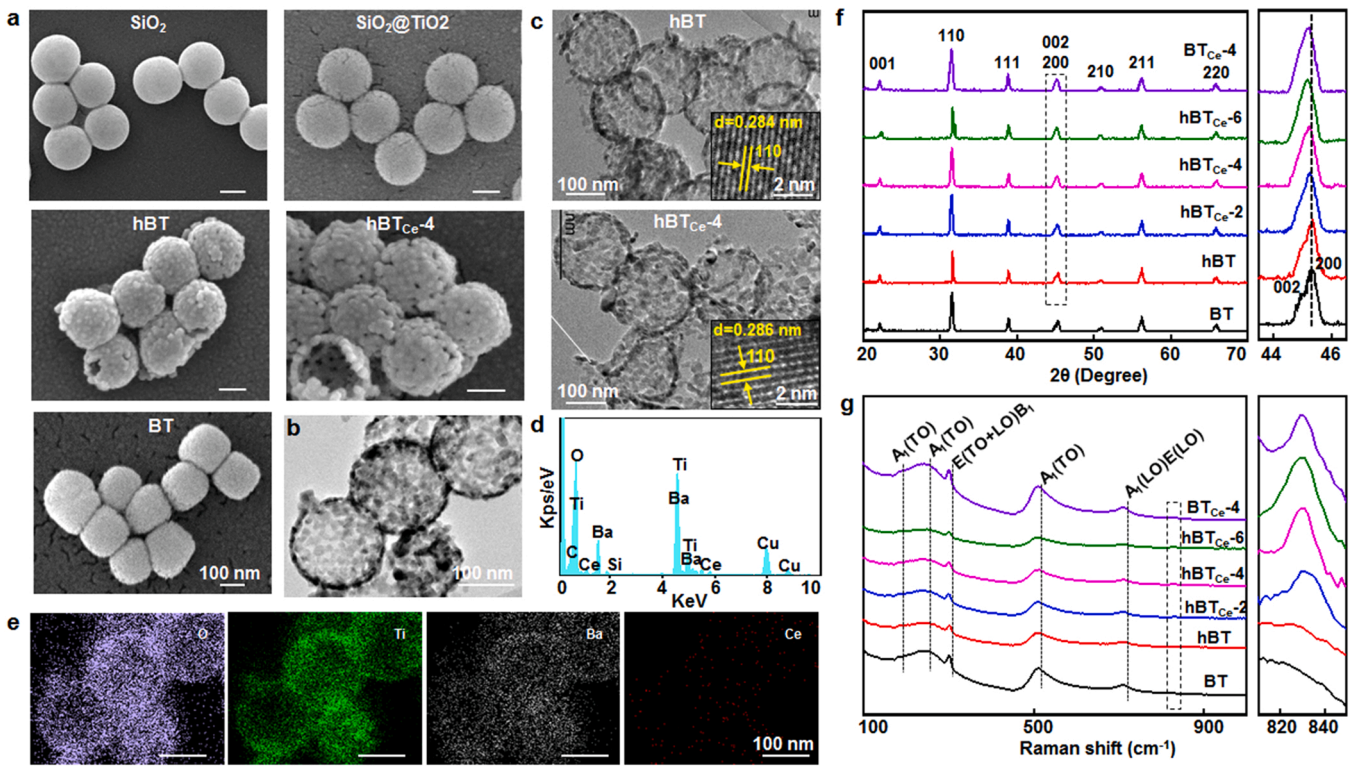

Fig. 1. Characterization of hBT_{Ce} NPs. (a) SEM images of SiO_2, SiO_2/TiO_2, hBT, hBT_{Ce}, and BT NPs. (b) TEM image of hBT_{Ce} NPs. (c) High-resolution TEM images of hBT and hBT_{Ce} NPs (Inset shows the lattice fringe spacing). (d) EDX spectrum and (e) element mapping images of hBT_{Ce} NPs. (f) XRD and (g) Raman spectra of BT, hBT, hBT_{Ce}-2, hBT_{Ce}-4, hBT_{Ce}-6, and BT_{Ce}-4 NPs.

deformation and macroscopic polarization of NPs produced piezoelectric output. The piezoelectric potential promoted the redox reaction of e^- and h^+ on the NP surface with the surrounding O_2 and H_2O to generate ROS. The effect of hollow structure and Ce doping on the piezocatalytic activity of hBT_{Ce} NPs were investigated through degradation of MB, DPBF, and terephthalic acid as the probe molecules of ROS, $^1O_2/\bullet O^{2-}$, and •OH, respectively. Fig. 2a shows absorbance spectra of MB solutions after treatment with hBT_{Ce} NPs and ultrasonication for 10 min. BT/US treatment decreased the absorbance of MB solutions by 17.9%, and the generation of hollow structure enhanced the piezocatalytic activity of hBT/US with 42.6% of MB degradation (Fig. 2b). DPBF could be bleached by $^1O_2/\bullet O^{2-}$ with decreases in the absorbance at 420 nm [40].

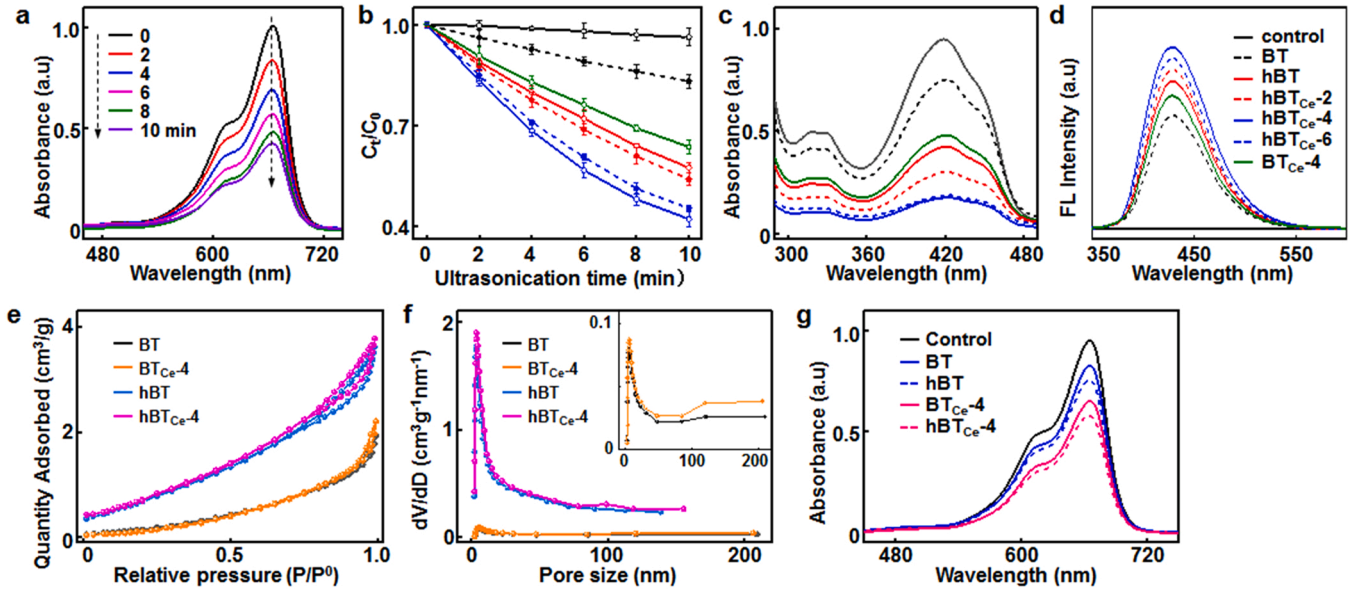

Fig. 2. ROS generation of hBT_{Ce} NPs. (a) Time-dependent degradation of MB by hBT_{Ce}-4 NPs under ultrasonication for different time periods. (b) Degradation rate of MB by BT, hBT, hBT_{Ce}-2, hBT_{Ce}-4, hBT_{Ce}-6, and BT_{Ce}-4 NPs under ultrasonication for 10 min, using ultrasonication only as the control ($n = 3$). (c) $^1O_2/\bullet O^{2-}$ generation by using DPBF as the probe and (d) •OH generation by using 2-hydroxyterephthalic acid as the probe after different treatments. (e) Nitrogen adsorption–desorption isotherm and (f) pore size distribution of BT, hBT, BT_{Ce}-4, and hBT_{Ce}-4. (g) Degradation of MB after treatment with of BT/BT_{Ce}-4 (1.0 mg/mL) and hBT/hBT_{Ce}-4 (0.38 mg/mL) NPs with the same BET surface areas under ultrasonication for 10 min, using ultrasonication only as the control.

As shown in Fig. 2c, hBT/US treatment promoted the generation of $^1O_2$/•O^{2-}, and the decrease in the DPBF absorbance exhibited 2.4-fold higher than that of BT/US. Nonfluorescent terephthalic acid could be oxidized by •OH into highly fluorescent 2-hydroxyterephthalic acid [40]. The increase in the fluorescence intensity after hBT/US treatment was nearly twice that of BT/US (Fig. 2d).

Hollow nanomaterials often have large specific surface area, and the large contents of active sites should promote the piezocatalytic activity. Fig. 2e shows the nitrogen adsorption/desorption isotherms, and the BET surface area of hBT (41.6 m^2/g) was significantly higher than that of BT NPs (13.3 m^2/g). Fig. 2f displays the BJH pore size distribution and the average pore size of hBT (14.2 nm) was much larger than that of BT (8.3 nm). To exclude the effect of surface areas, MB degradation was performed after treatment with BT (1.0 mg/mL) and hBT (0.38 mg/mL) NPs with the same BET surface areas, showing a stronger degradation effect of hBT after 10 min of ultrasonication (Fig. 2g). Thus, in addition to the large surface area, the high piezoelectric potential of hollow NPs should play an important role in the piezocatalytic activity.

To verify the effect of hollow structure, the distribution of piezoelectric potential of BT and hBT are simulated through FEM by using COMSOL Multiphysics. The model dimensions of NPs were similar to the real dimensions shown in TEM (Fig. 1b, c). Fig. 3a displays the induced surface piezoelectric potential under the pressure of 10^8 Pa on BT (0.13 V) and hBT NPs (0.91 V). In addition, the induced surface piezoelectric potential was simulated under different pressures, and the differences between BT and hBT NPs increased with the loading pressures (Fig. 3b). The induced surface piezoelectric potential of hBT is nearly 7 times higher than that of BT with increasing the pressure to 10^8 Pa, suggesting the significantly higher piezoelectric coefficient of hBT. PFM measurement was further performed to investigate the effect of hollow structure, and the different contrasts of the PFM phase and amplitude images represented the direction of ferroelectric polarization and the strength of piezoelectric response [16]. As shown in Fig. 3c, BT and hBT NPs showed a clear spheric morphology with a size of about 200 nm, which was consistent with those in SEM and TEM images (Fig. 1). Compared to those of BT, the phase image (Fig. 3d) and PFM amplitude image (Fig. 3e) of hBT NPs had more clear outlines and matched well with the morphological image. It was indicated that under the same voltage, the volume change of hBT was larger and had a stronger piezoelectric response [16].

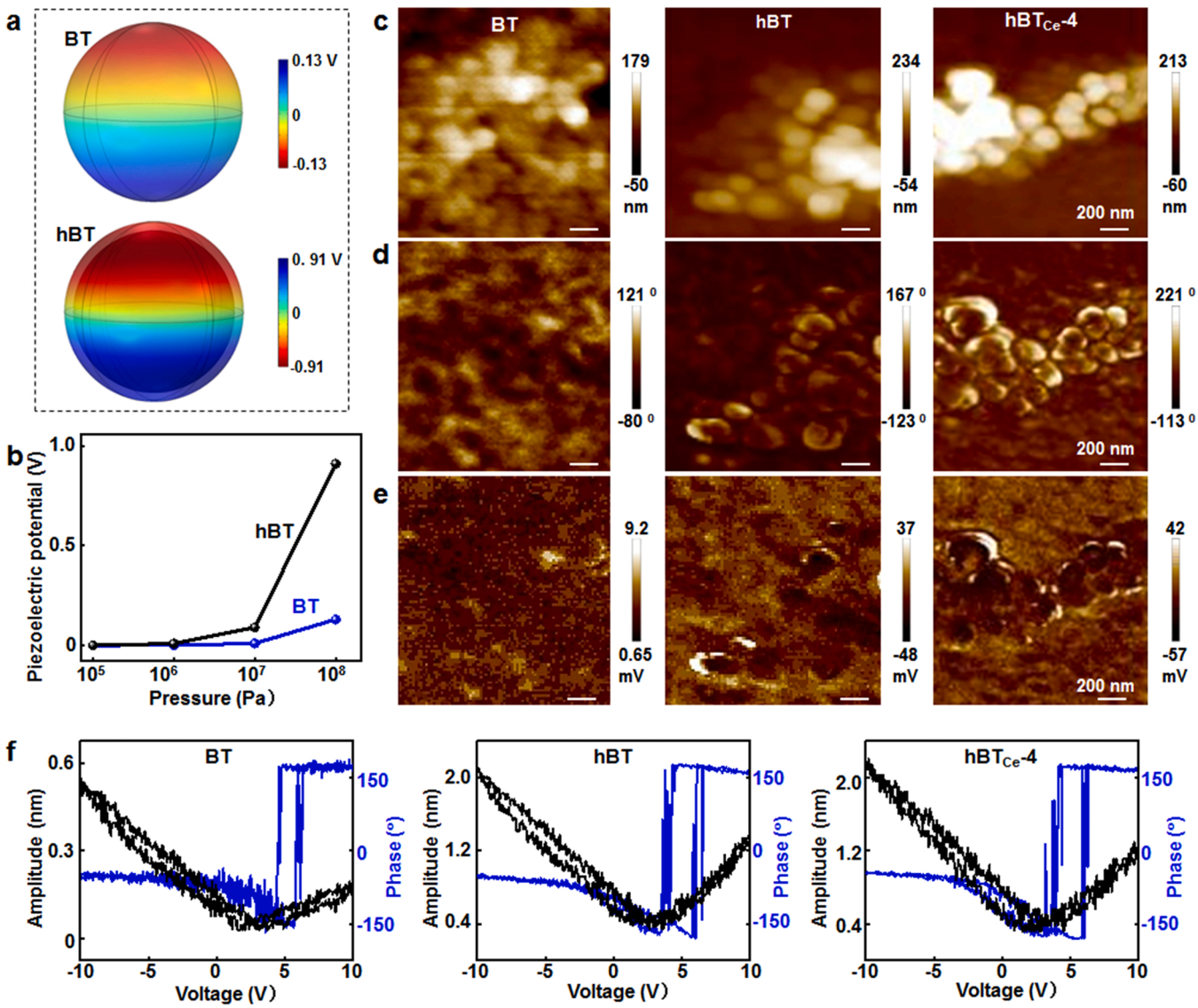

Fig. 3. Piezocatalytic activity of hBT_{Ce} NPs. (a) COMSOL simulated piezoelectric potential distribution on the surface of BT and hBT NPs under the cavitation pressures of 10^8 Pa, (b) Surface piezoelectric potential of BT and hBT NPs under different pressures from 10^5 to 10^8 Pa. (c) Topography image, (d) amplitude image, (e) phase image, and (f) displacement-voltage butterfly loop and phase hysteresis loop of BT, hBT, and hBT_{Ce}-4 NPs.

Fig. 3f shows the amplitude-voltage butterfly loops and well-defined 180° phase of change hysteresis loops under a reversal field of 10 V. As indicated in the amplitude-voltage butterfly loops, BT and hBT had the maximum amplitudes of about 0.72 and 2.06 nm, respectively. The piezoelectric coefficient (d_{33}) referred to the ratio of the electric field strength to the stress change when varied stresses were applied to the piezoelectric NPs. The d_{33} values could be acquired through calculating the corresponding slope of the Displacement-Voltage curve according to Eq. (2) [41]:

$$d_{33} = (A-A_0)/(V-V_0) \quad (2)$$

Where V and A represent the applied voltage and amplitude respectively; V_0 and A_0 are the intersection point of the amplitude butterfly loop curve. The hollow structure caused 2.6 folds larger d_{33} values for hBT (129.9 pm/V) than that of BT NPs (49.2 pm/V).

3.3. Effect of Ce doping on the piezocatalytic activity of hBT_{Ce} NPs

To demonstrate the effect of Ce doping, different amount of Ce $(NO_3)_3 \bullet 6\ H_2O$ was used to prepare hBT_{Ce} NPs, and the Ce levels were set at 2% (hBT_{Ce}-2), 4% (hBT_{Ce}-4), and 6% (hBT_{Ce}-6). As shown in Fig. 2c, the Ce doping in hBT NPs promoted MB degradation, and the ROS generation of hBT_{Ce}-4 NPs was significantly higher than those of hBT (1.4 folds), hBT_{Ce}-2 (1.3 folds) and hBT_{Ce}-6 (1.1 folds) after ultrasonication for 10 min. The analysis with DPBF and terephthalic acid probes also showed similar results in the generation of $^1O_2/^{\bullet}O^{2-}$ (Fig. 2c) and •OH (Fig. 2d). The Ce doping in hBT NPs showed no effect on the specific surface areas (Fig. 2e) and average pore sizes (Fig. 2f). To clarify the effect of Ce doping on the piezocatalytic activity, the lattice distortion and the change of OV amount were examined by PFM and XPS analysis. The topography (Fig. 3c), PFM amplitude (Fig. 3d) and phase image (Fig. 3e) of hBT_{Ce}-4 NPs showed stronger piezoelectric response than hBT. As shown Fig. 3f, the maximum amplitude of the amplitude-voltage butterfly loops of hBT NPs increased from 2.06 to 2.15 nm after

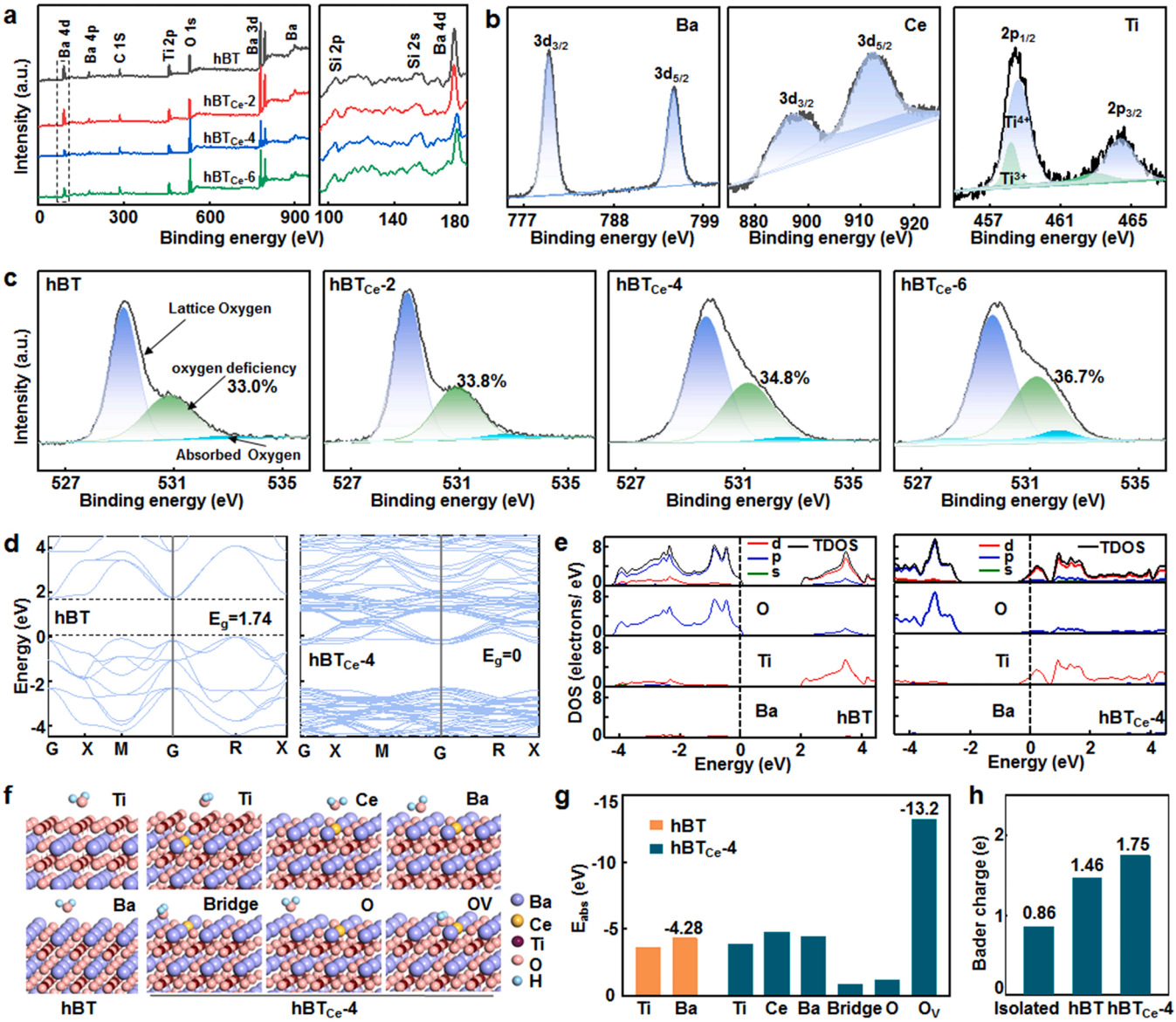

Fig. 4. Characterization of Ce doping in hBT_{Ce} NPs. (a) XPS spectra and the magnified peak of BT, hBT_{Ce}-2, hBT_{Ce}-4, and hBT_{Ce}-6 NPs. (b) High-resolution XPS spectra of Ba 3d, Ce 3d, and Ti 2p of hBT_{Ce}-4 NPs. (c) High-resolution XPS spectra of O 1 s of different NPs. (d) Calculated band energy and (e) DOS of hBT and hBT_{Ce}-4 NPs to reveal OVs. (f) H_2O adsorption model and (g) adsorption energy on the Ti and Ba sites of hBT and the Ti, Ba, Ce, O, OV and bridge sites of hBT_{Ce}-4 NPs. (h) Bander charge of the isolated H_2O, H_2O at the Ba site on hBT NPs and the OV site on hBT_{Ce}-4 NPs.

Ce doing. This result demonstrated an appropriate amount of Ce doping could promote the polarization, enhance the piezoelectric response and increase the d_{33} value (132.1 pm/V), which was consistence with the XRD result (Fig. 1f).

XPS was used to analyze chemical states of each element, and all the NPs displayed similar spectra composing of Ba 3d (779 and 794 eV), Ti 2p (458 and 464 eV), O 1 s (530 eV) and C 1 s (286.3 eV) peaks (Fig. 4a). The tiny peaks at 105 eV (Si 2 s) and 153 eV (Si 2p) suggested the efficient removal of SiO_2 cores and formation of a hollow structure. Fig. 4b illustrates the high-resolution XPS spectra of Ba 3d, Ce 3d, Ti 2p, and O 1 s for hBT_{Ce}-4 NPs. The characteristic peaks at 795.4 and 780.1 eV were ascribed to Ba atoms in the perovskite structure of Ba $3d_{3/2}$ and Ba $3d_{5/2}$, respectively [42]. The XPS spectrum of Ce^{3+} showed $3d_{3/2}$ (902.8 eV) and $3d_{5/2}$ (888.2 eV) peaks, verifying that Ce^{3+} ions were doped into the perovskite framework of hBT_{Ce}-4 NPs without generation of CeO_2 [43]. Ti elements showed two peaks at 464.3 (Ti $2p_{1/2}$) and 458.5 eV ($2p_{3/2}$). Ti^{4+} showed peaks centered at 458.1 and 464.4 eV, while those at 458.8 and 462.6 eV belonged to Ti^{3+}. The change from Ti^{4+} to Ti^{3+} in the vicinal Ti ions caused the formation of OVs to maintain the local charge balance [44].

The content of OVs in Ce-doped BT NPs was calculated from the peak fitting of O 1 s spectra. As shown in Fig. 4c, the O 2p peak at ~ 529.8 eV corresponded to the lattice oxygen, and the peaks at ~ 531.0 and 532.4 eV were attributed to the oxygen vacancy and surface adsorption of oxygen [45]. As the Ce content increased, the concentration of OVs gradually increased from 33.0% (hBT) to 33.8% (hBT_{Ce}-2), 34.8% (hBT_{Ce}-4), and 36.7% (hBT_{Ce}-6). In general, the generation of OVs decreased the electronegativity and electron cloud around oxygen atoms, diminished the shielding effect, and elevated the binding energy of oxygen atoms, which were beneficial to the catalytic reaction [11]. Thus, the optimal piezocatalytic activity of hBT_{Ce}-4 NPs was resulted from the lattice distortion and the change of OV contents regulated by Ce doping.

DFT modeling and simulation were employed to confirm the origin of Ce doping-induced OVs on the separation effectiveness of e^-/h^+ pairs created by the piezoelectric effect. Fig. 4d shows the calculated band structure of hBT and hBT_{Ce}-4 NPs with a Ce doping level of 4%. The top of valence band and the bottom of conduction band of hBT NPs were both at G point, which produced a direct band structure and showed semiconductivity with a band gap of 1.74 eV in the spin up channel. The experimental band gap of hBT NPs was higher than the estimated one, which was attributed to the ignorance of mutual repulsion and strong correlation between electrons in the same spin orbit [46]. However, the Ce doping generated OVs in hBT_{Ce}-4 NPs, and the Fermi level crossed the conduction band, thus the band gap should be 0. Thus, the reduced band gap suggested a higher catalytic efficacy of hBT_{Ce}-4 than that of hBT [11].

The bonding and electronic states of different atoms and energy levels could be predicted form the partial DOS [47]. The negative and positive values on the X axis corresponded to the valence and conduction bands, respectively. Fig. 4e shows the total DOS for hBT and hBT_{Ce}-4 NPs and the partial DOS for different atoms. The valence and conduction bands of hBT NPs were originated from the O 2p and Ti 3d orbitals, respectively. The oxygen deficiency decreased the DOS at the conduction band and the band gap, indicating that electrons in hBT_{Ce}-4 with OVs had stronger feasibility to transition from valence to conduction bands.

To clarify the effect of OVs on the catalytic activity, DFT calculations were performed to clarify the adsorption and activation of H_2O on the pure and OVs-filled BT [26]. OVs of hBT_{Ce}-4 were generated by removal of oxygen atoms from the 001 surface of hBT. Fig.4f summarizes H_2O adsorption models on the Ti and Ba sites of hBT and the Ti, Ba, Ce, O, OV and bridge sites of hBT_{Ce}-4 NPs. As seen from Fig. 4g, the adsorption energies of H_2O on the Ba site of hBT (−4.28 eV) was greater than that on the Ti site (−3.56 ev). The adsorption energy on the OV site (−13.2 ev) of hBT_{Ce}-4 surface was significantly higher than those on the other sites, indicating that H_2O molecules were mainly adsorbed on the OVs. Compared to that of hBT, the higher adsorption energy on hBT_{Ce}-4 NPs indicated that the OVs facilitated H_2O adsorption. In addition, a higher adsorption energy suggested a lower Gibbs free energy for H_2O oxidization. The O—H bond lengths of H_2O on the Ba site of hBT were 0.978 and 0.982 Å with a minor change compared to free H_2O [11]. However, the O—H bond lengths of H_2O confined by the OV site of hBT_{Ce}-4 were 1.010 and 0.996 Å, which were obviously elongated compared to that of hBT. Fig. 4h indicates the Bader charge results of H_2O at the Ba site on hBT (1.46 e) and the OV site on hBT_{Ce}-4 NPs (1.75 e). The rupture of Ti-O bonds on the hBT_{Ce}-4 surface caused Ti atoms to provide more extra electrons to the oxygen atoms of H_2O, indicating that the OVs contributed to O-H bond breakage in H_2O. Thus, DFT calculation verified that the OVs on hBT_{Ce}-4 surface significantly promoted H_2O adsorption, H-O bond activation and ROS generation.

These above results indicated that OVs induced by Ce doping on hBT crystal lattice regulated the piezocatalytic performance. At a low Ce doping level, hBT_{Ce}-2 NPs had a low concentration of OVs and could maintain a large piezoelectric property and generate a large piezoelectric potential to accelerate the charge transfer. But the weak adsorption of O_2 and H_2O and easy recombination of the activated e^-/h^+ pairs led to a limited piezocatalytic activity. hBT_{Ce}-6 NPs with a high concentration of OVs could absorb abundant O_2 and H_2O, and enhanced the separation of the activated e^-/h^+ pairs, but the high concentration of OVs usually caused structural transformation of piezoelectric materials and weakened the piezoelectric properties. Thus, the OV content caused by Ce doping was essential to improve the piezocatalytic performance.

3.4. Piezocatalytic mechanism of hBT_{Ce} NPs

The piezocatalytic mechanism of hBT_{Ce}-4 NPs were examined in terms of photoluminescence spectra, piezoelectric current density and EIS analysis. Fig. 5a displays photoluminescence spectra to reflect the e^-/h^+ combination efficiency. The photoluminescence intensity of hBT indicated a larger increase than that of BT, which was due to the multiple reflections of the excitation light in the walls of hBT [48]. The photoluminescence spectra of hBT_{Ce} NPs with different Ce doping contents showed similar profiles and hBT_{Ce}-4 had the lowest fluorescence intensity, indicating the low e^-/h^+ pair recombination and high catalytic activity.

Fig. 5b summarizes the piezoelectric current density of NPs under ultrasonication. hBT_{Ce}-4 NPs generated the piezoelectric current density of 3.0 mA/cm^2, which was much higher than those of hBT_{Ce}-6 (2.8 mA/cm^2), hBT_{Ce}-2 (2.3 mA/cm^2), hBT (2.1 mA/cm^2), BT_{Ce}-4 (0.9 mA/cm^2), and BT (0.6 mA/cm^2) NPs ($p < 0.05$). It was indicated that the hollow structure enhanced the piezoelectric potential, and the OVs induced by Ce doping were beneficial to the separation of e^-/h^+ pairs. Fig. 5c shows EIS of different NPs, and the doping with a proper amount of Ce could reduce the electrical impedance, thereby favoring the charge transfer.

To interpret the high piezocatalytic efficacy of hBT_{Ce}-4 NPs, UV-Vis diffuse reflectance absorption spectra were recorded (Fig. 5d), and the band gap (E_g) was calculated according to the Kubelka-Munk function Eq. (3) [11]:

$$\alpha h\upsilon = A\,(h\upsilon - E_g)^2 \tag{3}$$

where α, $h\upsilon$, and A are the absorption coefficient, photon energy, and light absorption coefficient, respectively. The band gap of BT NPs was around 3.12 eV (Fig. 5e), which was basically consistent with the reported values [49]. The slightly lower band gap (3.06 eV) of hBT was attributed to the accompanied OVs in the hollow NPs with a thinner shell structure [50]. hBT_{Ce}-4 had a much lower band gap (2.89 eV), suggesting that the Ce doping enhanced the generation of OVs. The OVs may induce the variable valence state of Ti^{3+} and Ti^{4+} to inhibit the recombination of e^-/h^+ pairs. On the other hand, the low band gap of hBT_{Ce}-4 NPs meant to be easily bent under pressure, thereby producing

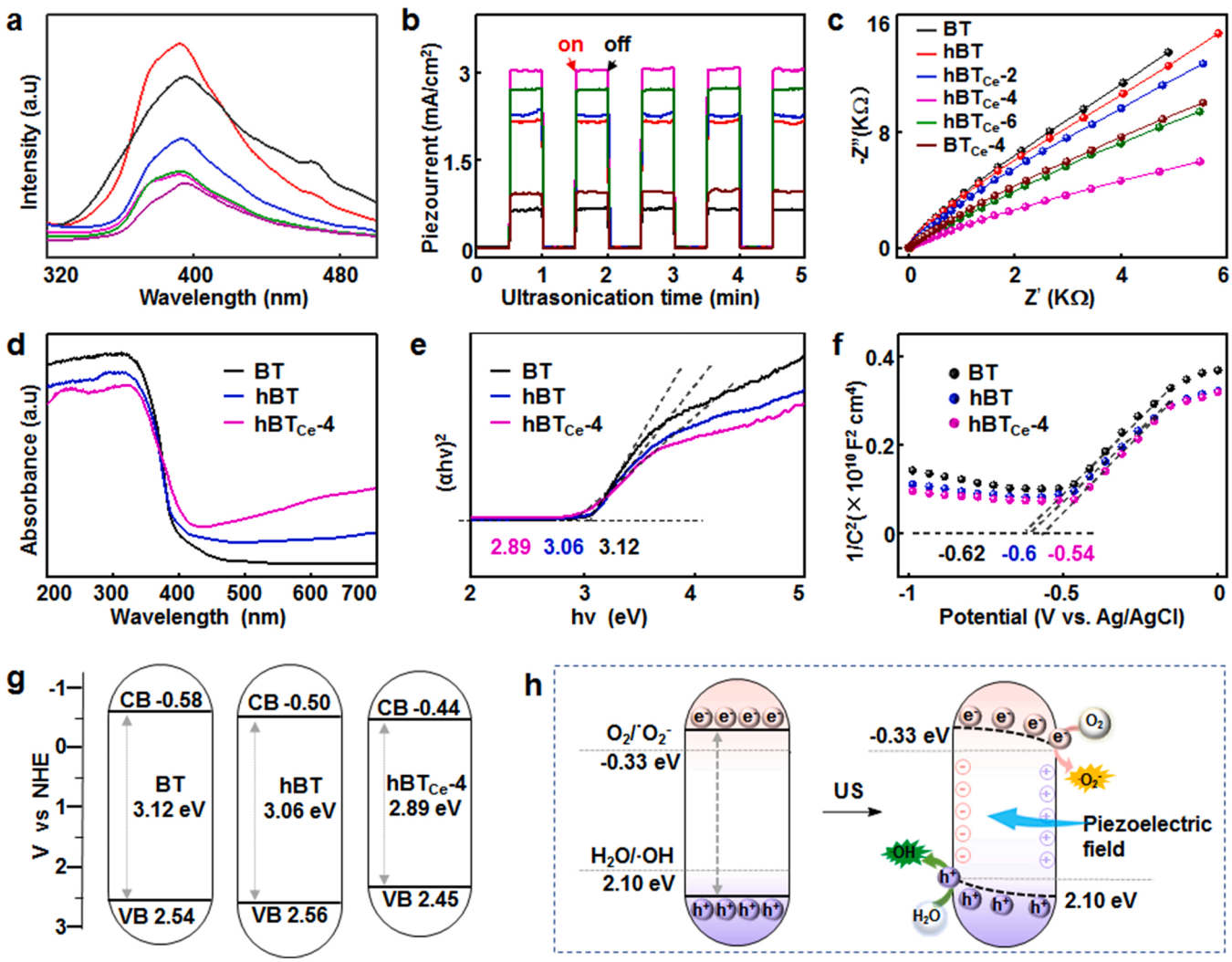

Fig. 5. Piezocatalytic mechanism clarification of hBT_{Ce} NPs under ultrasonication. (a) Photoluminescence spectra, (b) piezoelectric current response curves under cycled ultrasonication, and (c) EIS spectra of BT, hBT, hBT_{Ce}-2, hBT_{Ce}-4, hBT_{Ce}-6, and BT_{Ce}-4 NPs. (d) UV–Vis diffuse reflectance spectra, (e) Kubelka–Munk plots according to UV–Vis diffuse reflectance spectroscopy, (f) Mott-Schottky plots, and (g) schematic illustration of the intrinsic band structure of BT, hBT, and hBT_{Ce}-4 NPs. (h) Schematic illustrations on the tilted energy bands under piezoelectric field to facilitate the production of·O^{2-} and·OH.

more ROS.

The type of semiconductor and its position of the band edge were critical to the catalytic performance, and thus the Mott−Schottky plots of BT, hBT, and hBT_{Ce}-4 were drafted to identify the semiconductor type and the flat band energy potential [39]. As shown in Fig. 5f, the positive slopes indicated an n-type semiconductor nature, where the flat band potential was about 0.1 V below the conduction band potential. The flat band potential was determined by making a tangent to the straight part of the plot to form an intersection with the X-axis, and those of BT, hBT, and hBT_{Ce}-4 NPs were − 0.68, − 0.60, and − 0.54 V, respectively. Thus, the conduction band (E_{CB}) potentials of BT, hBT, and hBT_{Ce}-4 NPs were estimated to be − 0.58, − 0.5, and − 0.44 V, respectively. Fig. 5g summarizes energy band positions of BT, hBT, and hBT_{Ce}-4 according to Eq. (4):

$$E_g = E_{VB} - E_{CB} \tag{4}$$

where the valence band (E_{VB}) was calculated to be 2.54, 2.56, and 2.45 V for BT, hBT, and hBT_{Ce}-4 NPs, respectively. Compared with those of BT and hBT NPs, the conductive and valent bands of hBT_{Ce}-4 were closer to the standard redox potential (vs NHE) of $\bullet O^{2-}/O_2$ (−0.33 V) and •OH/ H_2O (+2.10 V), which meant that hBT_{Ce}-4 NPs could more easily separate e^-/h^+ pairs and generate ROS [40]. Fig. 5h depicts the piezocatalytic mechanism of hBT_{Ce}-4 NPs. As a ferroelectric material, the charges on the surface of hBT_{Ce}-4 NPs were usually neutralized with free charges in the solution at a stress-free sate. hBT_{Ce}-4 NPs with a non-centrosymmetric structure were deformed under ultrasonication, resulting in an internal electric field and surface piezoelectric potential. Under the action of piezoelectric potential, the valence and conduction bands of NPs were tilted, which were more conducive to the separation of free charges (e^-/h^+) to the material surface. Subsequently e^- and h^+ reacted with O_2 and H_2O on the material surface to form $\bullet O^{2-}$ and •OH. Therefore, the surface piezoelectric potential, energy band position, charge separation property, and the adsorption of O_2 and H_2O would determine the piezocatalytic activity of NPs.

Thus, we speculate that the piezocatalytic activity of hBT_{Ce}-4 NPs was enhanced through several mechanisms. In addition to the high surface area and mesoporous structure of hollow hBT_{Ce}-4 NPs that could provide abundant active sites for the catalytic reaction, the first contributor was the hollow structure to increase in the surface piezoelectric potential. The two-dimensional walls of hollow NPs indicated a high strain coefficient for piezoelectric output compared with solid NPs. Compared with two-dimensional nanosheets, the three-dimensional network structures could provide a robust stability, which not only prevented the aggregation and degradation of reaction sites, but also

maintained the high activity of surface sites [51]. Second, Ce doping would induce the lattice distortion of hBT and enhance the spontaneous polarization, thereby increasing the piezoelectric potential. the Ce dopants had a narrower band gap, which was beneficial to the excitation of electrons and improved the catalytic activity. Third, Ce doping-induced OVs could regulate the charge density distribution, which greatly promoted the further separation of the activated e^-/h^+ pairs for a high catalytic activity. OVs enhanced the adsorption and activation of O_2 and H_2O to lower the energy barrier of redox. Previous study has showed that OVs could reduce the piezoelectric response, but appropriate OVs would greatly promote the piezocatalytic activity [16]. Excessive vacancies caused by the overdosed Ce dopants might change the crystal structure of NPs and became new charge recombination centers, thus reducing the piezoelectric catalytic performance [11]. Therefore, the optimal doping amount of Ce in hBT should achieve a balance in improving the piezoelectric performance, narrowing the band gap, providing appropriate OVs for piezocatalysis, and avoiding the impact of excessive OVs on the piezoelectric performance.

3.5. Antibacterial efficacy of hBT_{Ce} NPs

Piezoelectric NPs generate a piezoelectric field under pressure, and the current may depolarize bacterial membrane and reduce membrane stability and ROS tolerance. The antibacterial efficacy of NPs was investigated after incubation with *P. aeruginosa* and MRSA, and Fig. 6a shows bacterial viabilities after hBT_{Ce}-4/US treatment, using hBT/US, BT/US and BT_{Ce}-4/US as controls. All the NPs showed a concentration-dependent antibacterial effect, and *P. aeruginosa* and MRSA were almost fully destroyed by hBT_{Ce}-4 at around 25 μg/mL after ultrasonication for 5 min. Recently Lei et al. introduced OVs in tBT NPs through sulfur doping to improve the piezoelectric properties and reduce the recombination of e^-/h^+ pairs; An antibacterial efficiency of 97% was detected against *S. aureus* at the NP concentration of 200 μg/mL after ultrasonication for 15 min [52]. Wang et al. doped Ca and Zr in tBT and the OV generation exhibited almost full destruction of *S. aureus* after treatment with NPs at 1 mg/mL after ultrasonication for 45 min [53]. The significant antibacterial efficacy of hBT_{Ce}-4/US at a much lower NP dose (25 μg/mL) and shorter ultrasonication (5 min) indicated that both the hollow structure and Ce doping significantly improved the piezoelectric antibacterial properties of BT NPs.

The standard plate counting was used to examine the antibacterial efficacy of NPs at the concentration of 25 μg/mL (Fig. 6b), showing similar antibacterial effect to *P. aeruginosa* and MRSA. Compared with no viable bacteria after hBT_{Ce}-4 treatment, abundant viable MRSA still existed after treatment with BT (54.3%), BT_{Ce}-4 (21.6%), hBT (19.9%), hBT_{Ce}-2 (6.8%), and hBT_{Ce}-6 (0.8%) NPs ($p < 0.05$). Fig. 6c displays surface morphologies of *P. aeruginosa* and MRSA after treatment with hBT_{Ce}-4/US. Compared with pristine bacteria, a certain degree of damaged and deformed membranes was observed on both *P. aeruginosa* and MRSA. The micro-electric field on the surface of piezoelectric NPs produced ROS to damage bacterial membranes, lead to leakage of cell contents and ultimately cause bacterial death.

The depolarization of bacterial membrane was detected by using DiBAC4(3) as a membrane potential probe. The dye was excluded from polarized bacteria due to the negative charge, but could enter depolarized bacteria and bind to intracellular proteins or membranes, emitting strongly fluorescence [29]. Fig. 6d summarizes fluorescence intensities of bacterial suspensions after treatment with different NPs and ultrasonication. hBT_{Ce}-4/US treatment showed the highest fluorescence intensity, indicating the highest DiBAC4(3) concentration in the cytoplasm and the strongest depolarization of bacterial inner membranes. The difference in the fluorescence intensities between *P. aeruginosa* and MRSA was mainly related with the structure of the outermost membrane. Compared with gram-negative *P. aeruginosa*, the outermost layer of gram-positive MRSA contained a thicker and harder layer of peptidoglycan with teichoic acid groups, giving bacteria higher negatively charged surface and harder to be depolarized [54]. Thus, these results elucidated that the electrical stimulation promoted the

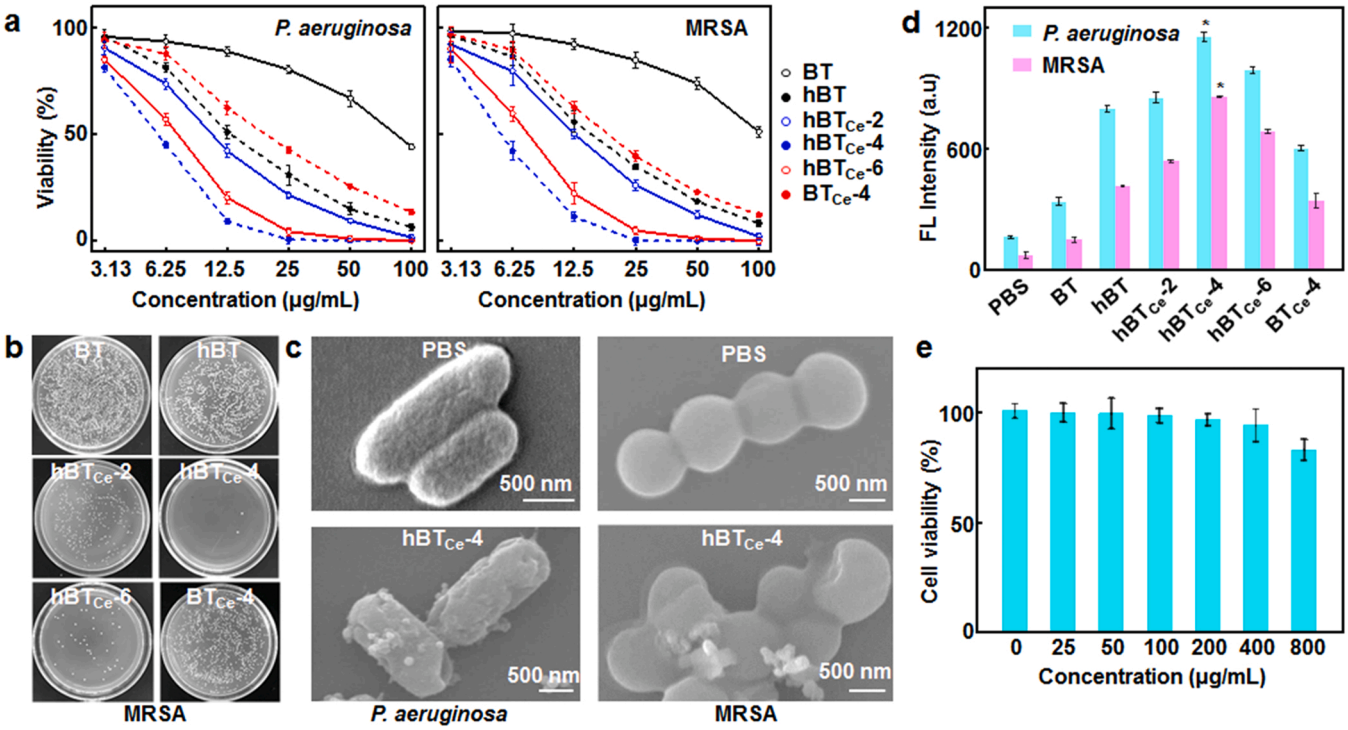

Fig. 6. Antibacterial activity of hBT_{Ce} NPs. (a) Viability of *P. aeruginosa* and MRSA after ultrasonication for 5 min of BT, hBT, hBT_{Ce}-2, hBT_{Ce}-4, hBT_{Ce}-6, and BT_{Ce}-4 NPs at different concentrations ($n = 5$). (b) Agar plate images for counting viable MRSA after different treatments. (c) SEM images of *P. aeruginosa* and MRSA after treatment with hBT_{Ce}-4 and PBS and ultrasonication for 5 min (d) Membrane potential changes of *P. aeruginosa* and MRSA after ultrasonication of different NPs ($n = 5$). (e) NIH-3T3 viability after BT_{Ce}-4 NP treatment at different concentrations ($n = 5$).

polarization of bacterial membranes, reduced the tolerance of bacteria to ROS and enhanced the bactericidal effect of ROS. It was suggested that the piezoelectric effect of NPs generated electric current and ROS to achieve a synergistic effect on the sterilization efficacy. In addition, the cytotoxicity of hBT_{Ce}-4 NPs was examined after incubation with NIH3T3 cells for 24 h, showing no obvious cytotoxicity even at a concentration of 800 μg/mL (Fig. 6e). It was indicated that NPs themselves had good biocompatibility and ensured further biomedical use.

3.6. Antibiofilm efficacy of hBT_{Ce} NPs

Clinically, over 70% of bacterial infections are related to biofilms, and the formation of bacterial biofilms blocks the interactions between antibiotics and bacteria, which is one of the key factors leading to bacterial resistance [55]. The antibiofilm ability of hBT_{Ce}-4/US was examined on MRSA biofilms in terms of biofilm mass and integrity and bacterial viability. Fig. 7a displays the crystal violet-stained images of biofilms, showing few biofilms remaining after hBT_{Ce}-4/US treatment. The stained crystal violet was dissolved in ethanol and the absorbance reflected the levels of remained biofilms [30]. As shown in Fig. 7b, hBT_{Ce}-4 treatment had an antibiofilm efficiency of 94.9%, which was significantly higher than those after BT (17.5%), BT_{Ce}-4 (58.3%), and hBT (65.2%) treatment ($p < 0.05$). Fig. 7c displays agar plate images for bacterial colony counting after different treatments, showing negligible bacteria in biofilms after hBT_{Ce}-4/US treatment. As shown in Fig. 7b, only 2.6% of bacteria were alive after hBT_{Ce}-4 treatment, and much more live bacteria were detected after BT (73.6%), hBT (28.9%), and BT_{Ce}-4 (32.7%) treatment ($p < 0.05$).

Fig. 7d displays SEM morphologies of the retrieved biofilms. Biofilms after PBS or BT treatment appeared dense and thick, and the bacteria were maintained typically spherical-shaped with smooth and intact cell walls. Only a small amount of bacterial membranes were destroyed after BT_{Ce}-4/US and hBT/US treatment, and sparse bacterial films were observed after hBT_{Ce}-4/US treatment. The bacterial surface appeared wrinkled and shrank, or even loss of cell membrane integrity and leakage of intracellular components. Bacterial viability in the retrieved biofilms was verified by CLSM, wherein the stained live bacteria emitted green fluorescence and dead bacteria were stained red (Fig. 7e). Compared with those without treatment, ultrasonication of biofilms showed negligible red fluorescence, indicating almost no antibacterial ability. BT_{Ce}-4/US and hBT/US treatment showed a stronger red staining of bacteria than those of BT/US, and negligible green fluorescence was observed after hBT_{Ce}-4/US treatment, suggesting almost no bacteria survival. It was indicated that hBT_{Ce}-4 NPs successfully ablated bacterial biofilms within a short period of ultrasonication, which was attributed to the large piezoelectric current (Fig. 5b) and high ROS generation efficiency (Fig. 2b).

4. Conclusion

We have developed a strategy of promote piezoelectric effect of BT NPs through simultaneous hollow structure and defect engineering. hBT_{Ce}-4 NPs were examined in terms of PFM observation, OV assay, electrochemistry measurement, and DFT/FEM-based simulation. The hollow structure induced a higher flexibility and surface piezoelectric potential under ultrasonication, a larger volume change under the same voltage, and a larger d_{33}. The introduced OVs after Ce doping narrowed the band gap, reduced the recombination of e^-/h^+ pairs, and enhanced the adsorption of O_2 and H_2O. hBT_{Ce}-4 NPs exhibited a much lower photoluminescence intensity, electrical impedance and band gap and a much higher piezoelectric current density than those of BT. Both the large piezoelectric current and high ROS generation efficiency contributed to the significant piezocatalytic activity, which enabled an efficient and safe non-antibiotic therapy of bacterial infections.

CRediT authorship contribution statement

Junwu Wei: Investigation, Methodology, Data curation, Writing –

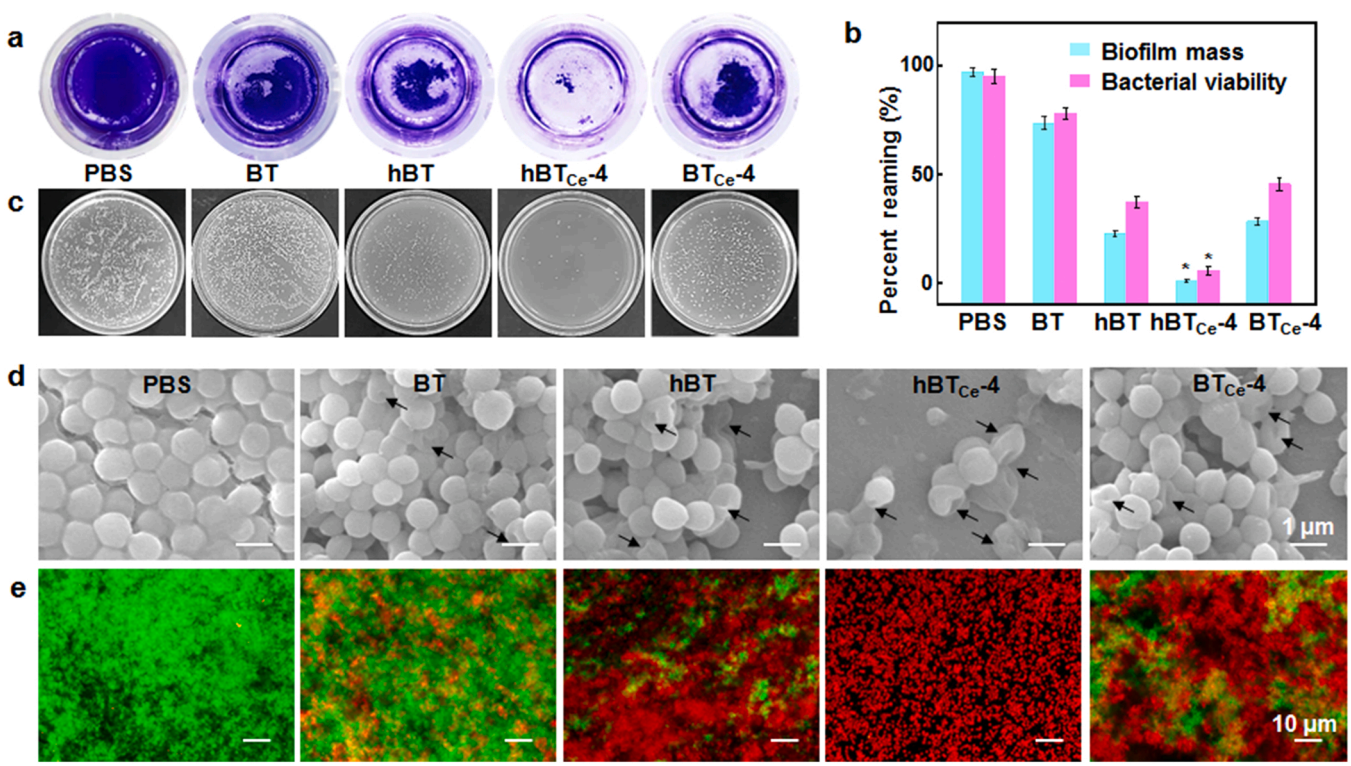

Fig. 7. Antibiofilm activity of hBT_{Ce} NPs. (a) Crystal violet-staining images of MRSA biofilms, (b) percentage residual biofilms and bacterial survival rates, (c) agar plate images for colony counting, (d) SEM images of biofilms and bacteria in the biofilms, and (e) CLSM images of live/dead-stained bacteria in the biofilms after treatment with BT, hBT, hBT_{Ce}-4, and BT_{Ce}-4 NPs at 25 μg/mL and ultrasonication for 5 min, using PBS treatment as the control ($n = 5$).

original draft. **Jing Xia:** Investigation, Data curation. **Xing Liu:** Investigation, Methodology. **Pan Ran:** Investigation, Methodology. **Guiyuan Zhang:** Investigation, Validation. **Chaoming Wang:** Investigation, Methodology, Validation. **Xiaohong Li:** Conceptualization; Investigation, Writing – review & editing, Funding acquisition, Project administration.

Declaration of Competing Interest

The authors declare that they have no known competing financial interests or personal relationships that could have appeared to influence the work reported in this paper.

Data Availability

Data will be made available on request.

Acknowledgements

This work is supported by the National Natural Science Foundation of China (32071394). We also thank the Analytical and Testing Center of Southwest Jiaotong University for SEM, TEM and CLSM analysis.

References

[1] I. Yelin, R. Kishony, Snap shot: Antibiotic resistance, Cell 172 (2018), 1136-1136.
[2] Y. Liu, L.Q. Shi, L.Z. Su, H.C. van der Mei, P.C. Jutte, Y.J. Ren, H.J. Busscher, Nanotechnology-based antimicrobials and delivery systems for biofilm-infection control, Chem. Soc. Rev. 48 (2019) 428–446.
[3] X. Fan, F. Yang, C.X. Nie, L. Ma, C. Cheng, R. Haag, Biocatalytic nanomaterials: a new pathway for bacterial disinfection, Adv. Mater. 33 (2021) 2100637.
[4] P. Ganguly, C. Byrne, A. Breen, S.C. Pillai, Antimicrobial activity of photocatalysts: fundamentals, mechanisms, kinetics and recent advances, Appl. Catal. B 225 (2018) 51–75.
[5] H. Hu, W. Feng, X.Q. Qian, L.D. Yu, Y. Chen, Y.H. Li, Emerging nanomedicine-enabled/enhanced nanodynamic therapies beyond traditional photodynamics, Adv. Mater. 33 (2021) 2005062.
[6] T. Wang, H. Chen, C. Yu, X. Xie, Rapid determination of the electroporation threshold for bacteria inactivation using a lab-on-a-chip platform, Environ. Int 132 (2019), 105040.
[7] T.X. Gu, Y. Wang, Y.H. Lu, L. Cheng, L.Z. Feng, H. Zhang, X. Li, G.R. Han, Z. Liu, Platinum nanoparticles to enable electrodynamic therapy for effective cancer treatment, Adv. Mater. 31 (2019) 1806803.
[8] Y. Long, H. Wei, J. Li, G. Yao, B. Yu, D.L. Ni, A.L.F. Gibson, X.L. Lan, Y.D. Jiang, W. B. Cai, X.D. Wang, Effective wound healing enabled by discrete alternative electric fields from wearable nanogenerators, ACS Nano 12 (2018) 12533–12540.
[9] Y.F. Wang, Y.M. Xu, S.S. Dong, P. Wang, W. Chen, Z.D. Lu, D.J. Ye, B.C. Pan, D. Wu, C.D. Vecitis, G.D. Gao, Ultrasonic activation of inert poly (tetrafluoroethylene) enables piezocatalytic generation of reactive oxygen species, Nat. Commun. 12 (2021) 3508.
[10] X.F. Zhou, F. Yan, A. Lyubartsev, B. Shen, J.W. Zhai, J.C. Conesa, N. Hedin, Efficient production of solar hydrogen peroxide using piezoelectric polarization and photoinduced charge transfer of nanopiezoelectrics sensitized by carbon quantum dots, Adv. Sci. 9 (2022) 2105792.
[11] D.M. Liu, J.T. Zhang, C.C. Jin, B.B. Chen, J. Hu, R. Zhu, F. Wang, Insight into oxygen-vacancy regulation on piezocatalytic activity of $(Bi_{1/2}Na_{1/2})TiO_3$ crystallites: experiments and first-principles calculations, Nano Energy 95 (2022), 106975.
[12] J. Wu, N. Qin, D.H. Bao, Effective enhancement of piezocatalytic activity of $BaTiO_3$ nanowires under ultrasonic vibration, Nano Energy 45 (2018) 44–51.
[13] P. Wang, L.L. Hao, Z.L. Wang, Y. Wang, M. Guo, P.B. Zhang, Gadolinium-doped BTO-functionalized nanocomposites with enhanced MRI and X-ray dual imaging to simulate the electrical properties of bone, ACS Appl. Mater. Interfaces 12 (2020) 49464–49479.
[14] C.Y. Yu, M.X. Tan, Y. Li, C.B. Liu, R.W. Yin, H.M. Meng, Y.J. Su, L.J. Qiao, Y. Bai, Ultrahigh piezocatalytic capability in eco-friendly $BaTiO_3$ nanosheets promoted by 2D morphology engineering, J. Colloid Interface Sci. 596 (2021) 288–296.
[15] W. Dong, H.Y. Xiao, Y.M. Jia, L. Chen, H.F. Geng, S.U. Bakhtiar, Q.Y. Fu, Y.P. Guo, Engineering the defects and microstructures in ferroelectrics for enhanced/novel properties: an emerging way to cope with energy crisis and environmental pollution, Adv. Sci. 9 (2022) 2105368.
[16] P.L. Wang, X.Y. Li, S.Y. Fan, X. Chen, M.C. Qin, D. Long, M.O. Tad, S.M. Liu, Impact of oxygen vacancy occupancy on piezo-catalytic activity of $BaTiO_3$ nanobelt, Appl. Catal. B 279 (2020), 119340.
[17] S. Lee, Highly uniform silica nanoparticles with finely controlled sizes for enhancement of electro-responsive smart fluids, J. Ind. Eng. Chem. 77 (2019) 426–431.
[18] L. Yu, H.B. Wu, X.W. Lou, Mesoporous $Li_4Ti_5O_{12}$ hollow spheres with enhanced lithium storage capability, Adv. Mater. 25 (2013) 2296–2300.
[19] X.F. Zhou, F. Yan, B. Shen, J.W. Zhai, N. Hedin, Enhanced sunlight-driven reactive species generation via polarization field in nanopiezoelectric heterostructures, ACS Appl. Mater. Interfaces 13 (2021) 29691–29707.
[20] J. Wu, Q. Xu, E.Z. Lin, B.W. Yuan, N. Qin, S.K. Thatikonda, D.H. Bao, Insights into the role of ferroelectric polarization in piezocatalysis of nanocrystalline $BaTiO_3$, ACS Appl. Mater. Interfaces 10 (2018) 17842–17849.
[21] W.Y. Dong, L. Li, X. Chen, Y.W. Yao, Y.K. Ru, Y.J. Sun, W.M. Hua, G.S. Zhuang, D. Y. Zhao, S.W. Yan, W.H. Song, Mesoporous anatase crystal-silica nanocomposites with large intrawall mesopores presenting quite excellent photocatalytic performances, Appl. Catal. B 246 (2019) 284–295.
[22] M.L. Song, Y. Cheng, Y. Tian, C.C. Chu, C. Zhang, Z.X. Lu, X.Y. Chen, X. Pang, G. Liu, Sonoactivated chemodynamic therapy: a robust ROS generation nanotheranostic eradicates multidrug-resistant bacterial infection, Adv. Funct. Mater. 30 (2020) 2003578.
[23] Y.Y. Yang, X.G. Zhang, C.G. Niu, H.P. Feng, P.Z. Qin, H. Guo, C. Liang, L. Zhang, H. Y. Liu, L. Li, Dual-channel charges transfer strategy with synergistic effect of Z-scheme heterojunction and LSPR effect for enhanced quasi-full-spectrum photocatalytic bacterial inactivation: new insight into interfacial charge transfer and molecular oxygen activation, Appl. Catal. B 264 (2020), 118465.
[24] X.Y. Huang, R. Lei, J. Yuan, F. Gao, C.K. Jiang, W.H. Feng, J.D. Zhuang, P. Liu, Insight into the piezo-photo coupling effect of $PbTiO_3$/CdS composites for piezo-photocatalytic hydrogen production, Appl. Catal. B 282 (2021), 119586.
[25] H. Ma, X.M. Wang, T.Q. Tan, X. Zhou, F. Dong, Y.J. Sun, Stabilize the oxygen vacancies in Bi_2SiO_5 for durable photocatalysis via altering local electronic structure with phosphate dopant, Appl. Catal. B 319 (2022), 121911.
[26] J. Bao, X.D. Zhang, B. Fan, J.J. Zhang, M. Zhou, W.L. Yang, X. Hu, H. Wang, B. C. Pan, Y. Xie, Ultrathin spinel-structured nanosheets rich in oxygen deficiencies for enhanced electrocatalytic water oxidation, Angew. Chem. -Int 54 (2015) 7399–7404.
[27] R. Su, Z.P. Wang, L.N. Zhu, Y. Pan, D.W. Zhang, H. Wen, Z.D. Luo, L.L. Li, F.T. Li, M. Wu, L.Q. He, P. Sharma, J. Seidel, Strain-engineered nano-ferroelectrics for high-efficiency piezocatalytic overall water splitting, Angew. Chem. -Int 60 (2021) 16019–16026.
[28] M. Cao, S. Wang, J.H. Hu, B.H. Lu, Q.Y. Wang, S.Q. Zang, Silver cluster-porphyrin-assembled materials as advanced bioprotective materials for combating superbacteria, Adv. Sci. 9 (2021) 2103721.
[29] M. Hasan, A. Nishimoto, T. Ohgita, S. Hama, H. Kashida, H. Asanuma, K. Kogure, Faint electric treatment-induced rapid and efficient delivery of extraneous hydrophilic molecules into the cytoplasm, J. Control. Release 228 (2016) 20–25.
[30] Q.Q. Deng, P.P. Sun, L. Zhang, Z.W. Liu, H. Wang, J.S. Ren, X.G. Qu, Porphyrin MOF dots–based, function-adaptive nanoplatform for enhanced penetration and photodynamic eradication of bacterial biofilms, Adv. Funct. Mater. 29 (2019) 1903018.
[31] M.H. Chen, B. Qiu, Z.L. Zhang, S. Xie, Y. Liu, T. Xia, X.H. Li, Light-triggerable and pH/lipase-responsive release of antibiotics and beta-lactamase inhibitors from host-guest self-assembled micelles to combat biofilms and resistant bacteria, Chem. Eng. J. 424 (2021), 130330.
[32] J. Fu, Y.D. Hou, M.P. Zheng, Q.Y. Wei, M.K. Zhu, H. Yan, Improving dielectric properties of PVDF composites by employing surface modified strong polarized $BaTiO_3$ particles derived by molten salt method, ACS Appl. Mater. Interfaces 7 (2015) 24480–24491.
[33] Z. Dai, F. Qin, H.P. Zhao, J. Ding, Y.L. Liu, R. Chen, Crystal defect engineering of aurivillius Bi_2MoO_6 by Ce doping for increased reactive species production in photocatalysis, ACS Catal. 6 (2016) 3180–3192.
[34] I.C. Amaechi, A.H. Youssef, D. Rawach, J.P. Claverie, S.H. Sun, A. Ruediger, Ferroelectric Fe-Cr codoped $BaTiO_3$ nanoparticles for the photocatalytic oxidation of azo dyes, ACS Appl. Nano Mater. 2 (2019) 2890–2901.
[35] J. Adam, G. Klein, T. Lehnert, Hydroxyl content of $BaTiO_3$ nanoparticles with varied size, J. Am. Ceram. Soc. 96 (2013) 2987–2993.
[36] L. Ju, T. Sabergharesou, K.G. Stamplecoskie, M. Hegde, T. Wang, N.A. Combe, H. Y. Wu, P.V. Radovanovic, Interplay between size, composition, and phase transition of nanocrystalline Cr^{3+}-doped $BaTiO_3$ as a path to multiferroism in perovskite-type oxides, J. Am. Chem. Soc. 134 (2012) 1136–1146.
[37] S.J. Liu, L.X. Zhang, J.P. Wang, Y.Y. Zhao, X. Wang, Abnormal curie temperature behavior and enhanced strain property by controlling substitution site of Ce ions in $BaTiO_3$ ceramics, Ceram. Int. 43 (2017), 14542-14542.
[38] H.-W. Lee, S. Moon, C.-H. Choi, D.K. Kim, Synthesis and size control of tetragonal barium titanate nanopowders by facile solvothermal method, J. Am. Ceram. Soc. 8 (2012) 2429–2434.
[39] Y.S. Dong, S.M. Dong, B. Liu, C.H. Yu, J. Liu, D. Yang, P.A.P. Yang, J. Lin, 2D piezoelectric Bi_2MoO_6 nanoribbons for GSH-enhanced sonodynamic therapy, Adv. Mater. 33 (2021) 2106838.
[40] Y. Nosaka, A.Y. Nosaka, Generation and detection of reactive oxygen species in photocatalysis, Chem. Rev. 117 (2017) 11302–11336.
[41] X.H. Meng, W. Wang, H. Ke, J.C. Rao, D.C. Jia, Y. Zhou, Synthesis, piezoelectric property and domain behaviour of the vertically aligned $K_{1-x}Na_xNbO_3$ nanowire with a morphotropic phase boundary, J. Mater. Chem. C 5 (2017) 747–753.
[42] W. Zhao, Q. Zhang, H.G. Wang, J.C. Rong, E. Lei, Y.J. Dai, Enhanced catalytic performance of $Ag_2O/BaTiO_3$ heterostructure microspheres by the piezo/pyro-phototronic synergistic effect, Nano Energy 73 (2020), 104783.
[43] K. Wu, Y.H. Sun, J. Liu, J.X. Xiong, J.L. Wu, J. Zhang, M.L. Fu, L.M. Chen, H. M. Huang, D.Q. Ye, Nonthermal plasma catalysis for toluene decomposition over $BaTiO_3$-based catalysts by Ce doping at A-sites: The role of surface-reactive oxygen species, J. Hazard. Mater. 405 (2021), 124156.

[44] D.H. Mei, X.B. Zhu, C.F. Wu, B. Ashford, P.T. Williams, X. Tu, Plasma-photocatalytic conversion of CO_2 at low temperatures: understanding the synergistic effect of plasma-catalysis, Appl. Catal. B 182 (2016) 525–532.
[45] Y.C. Wang, J.M. Wu, Effect of controlled oxygen vacancy on H_2-production through the piezocatalysis and piezophototronics of ferroelectric R_3C $ZnSnO_3$ nanowires, Adv. Funct. Mater. 30 (2020) 1907619.
[46] Y.N. Ma, H.M. Chen, F.C. Pan, Z.P. Chen, Z. Ma, X.L. Lin, F. Zheng, X.B. Ma, Electronic structures and optical properties of Fe/Co-doped cubic $BaTiO_3$, Ceram. Int. 45 (2019) 6303–6311.
[47] Q. Liu, F.Q. Zhan, H. Luo, D. Zhai, Z.D. Xiao, Q.W. Sun, Q.Y. Yi, Y. Yang, D. Zhang, Mechanism of interface engineering for ultrahigh piezo-photoelectric catalytic coupling effect of $BaTiO_3$@TiO_2 microflowers, Appl. Catal. B 318 (2022), 121817.
[48] L.B. Zong, J. Xu, S.Y. Jiang, K. Zhao, Z.M. Wang, P.R. Liu, H.J. Zhao, J. Chen, X. R. Xing, R.B. Yu, Composite yttrium-carbonaceous spheres templated multi-shell YVO_4 hollow spheres with superior upconversion photoluminescence, Adv. Mater. 29 (2017) 1604377.
[49] B. Yang, H.B. Chen, Y.D. Yang, L. Wang, J.H. Bian, Q.D. Liu, X.J. Lou, Insights into the tribo-/pyro-catalysis using Sr-doped $BaTiO_3$ ferroelectric nanocrystals for efficient water remediation, Chem. Eng. J. 416 (2021), 128986.
[50] J. Xiong, J. Di, J.X. Xia, W.S. Zhu, H.M. Li, Surface defect engineering in 2D nanomaterials for photocatalysis, Adv. Funct. Mater. 28 (2018) 1801983.
[51] W. Zhu, Z. Chen, Y. Pan, R.Y. Dai, Y. Wu, Z.B. Zhuang, D.S. Wang, Q. Peng, C. Chen, Y.D. Li, Functionalization of hollow nanomaterials for catalytic applications: nanoreactor construction, Adv. Mater. 31 (2019) 1800426.
[52] K. Wang, M.Q. Zhang, D.G. Li, L.H. Liu, Z.P. Shao, X.Y. Li, H. Arandiyan, S.M. Liu, Ternary BaCaZrTi perovskite oxide piezocatalysts dancing for efficient hydrogen peroxide generation, Nano Energy 98 (2022), 107251.
[53] J. Lei, C.F. Wang, X.B. Feng, L. Ma, X.M. Liu, Y. Luo, L. Tan, S.L. Wu, C. Yang, Sulfur-regulated defect engineering for enhanced ultrasonic piezocatalytic therapy of bacteria-infected bone defects, Chem. Eng. J. 435 (2022), 134624.
[54] J.P. Stratford, C.L. A.Edwards, M.J. Ghanshyam,D. Malyshev, M.A. Delise, Y. Hayashi, M. Asally, Electrically induced bacterial membrane-potential dynamics correspond to cellular proliferation capacity, Proc. Natl. Acad. Sci. U. S. A 116 (2019) 9552–9557.
[55] R.F. Landis, C.H. Li, A. Gupta, Y.W. Lee, M. Yazdani, N. Ngernyuang, I. Altinbasak, S. Mansoor, M.A.S. Khichi, A. Sanyal, V.M. Rotello, Biodegradable nanocomposite antimicrobials for the eradication of multidrug-resistant bacterial biofilms without accumulated resistance, J. Am. Chem. Soc. 140 (2018) 6176–6182.